\*CETTER STATE

## NASA TECHNICAL MEMORANDUM

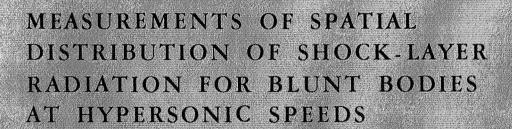


NASA TM X-852

(MASA-TM-X-852) ATASTREMETTS OF SPATIAL DISTRIBUTION OF SHOCK-LAYER PARIATION FOR BLURT BODIES AT HYPERSONIC SPEEDS J.J. Givens, et al (MASI) Jan. 1964 21 p

¥72-71536

Unclas 1/99 24444



by John J. Givens, Thomas N. Canning, and Harry E. Bailey

Ames Research Center Moffett Field, California

NATIONAL AERONAUTICS AND SPACE ADMINISTRATION . WASHINGTON, D. C. JANUARY 1964





## MEASUREMENTS OF SPATIAL DISTRIBUTION

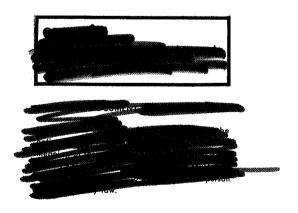
# OF SHOCK-LAYER RADIATION FOR BLUNT

## BODIES AT HYPERSONIC SPEEDS

By. John J. Givens, Thomas N. Canning, and Harry E. Bailey



Ames Research Center Moffett Field, California



NATIONAL AERONAUTICS AND SPACE ADMINISTRATION





#### NATIONAL AERONAUTICS AND SPACE ADMINISTRATION

### TECHNICAL MEMORANDUM X-852

MEASUREMENTS OF SPATIAL DISTRIBUTION OF SHOCK-LAYER

RADIATION FOR BLUNT BODIES AT HYPERSONIC SPEEDS\*

By John J. Givens, Thomas N. Canning, and Harry E. Bailey

#### SUMMARY

The relative intensity of radiation from the hot gas in the shock layer was measured for axisymmetric bodies with nose shapes ranging from a flat face to a hemisphere. Spatial resolution of the radiation was achieved using an image dissector, a device which optically scans strips across the model face. Data were obtained from models in free flight at velocities ranging from 5.5 to 8.2 kilometers per second and at free-stream densities of 0.013 and 0.065 standard atmosphere.

The results of the present measurements are compared directly with calculations of the radiation distribution based upon computation of shock-layer temperature and density and the available predictions of equilibrium thermal radiation of air. Good agreement is obtained, indicating that the distribution of equilibrium radiation in the shock layer about blunt bodies is well understood.

#### INTRODUCTION

The radiative heat transfer from the hot air in the shock layer to the stagnation point of bodies flying at hypersonic speeds has been studied extensively. Good correlation of radiation intensities has been achieved between analytic predictions based on shock-tube experiments and measurements made in ballistic ranges; values of the stagnation-point heating flux, deduced from measured total intensities from the shock layer, are available for the speed range from 4.5 to 13 kilometers per second (e.g., see refs. 1 and 2).

The application of this information to calculations of the radiative heating elsewhere on bodies is fairly straightforward, provided the shock shape and local gas properties can be estimated accurately throughout the shock layer. An example of this kind of estimation is found in reference 3 where Wick presents fairly extensive calculations for radiative heating flux across the faces of blunt axisymmetric bodies. His calculations are for shock layers in thermodynamic and chemical equilibrium and were made for a wide range of flight



conditions for bodies of varying bluntness ranging from hemispherical (R/d = 0.5) to R/d = 2.0. Here R is nose radius and d is body diameter at the body shoulder.

The purpose of the present work is to provide measurements of the distributions of radiative intensity as a function of position on blunt axially symmetric bodies. The data are compared directly with the calculations mentioned above. One shape not analyzed in Wick's paper, a flat-faced cylinder  $R/d=\infty$ , was also tested. Estimates of the distribution on this body, based on much the same numerical procedure as used in reference 3, are presented herein for comparison.

#### SYMBOLS

| $c_p$         | pressure coefficient  |  |  |  |  |  |  |  |  |  |
|---------------|---|--|--|--|--|--|--|--|--|--|
| đ             | body diameter at shoulder, cm   |  |  |  |  |  |  |  |  |  |
| F             | portion of total radiation to which the image dissector is sensitive                        |  |  |  |  |  |  |  |  |  |
| I             | radiation intensity, watts/cm <sup>2</sup>  |  |  |  |  |  |  |  |  |  |
| p             | pressure, dynes/cm <sup>2</sup>   |  |  |  |  |  |  |  |  |  |
| R             | nose radius, cm   |  |  |  |  |  |  |  |  |  |
| R <b>(</b> λ) | relative response of image dissector as a function of wave length                           |  |  |  |  |  |  |  |  |  |
| r             | radius of cross section   |  |  |  |  |  |  |  |  |  |
| <b>s</b>      | radial distance along body face from center, cm   |  |  |  |  |  |  |  |  |  |
| T             | temperature, <sup>O</sup> K   |  |  |  |  |  |  |  |  |  |
| T(y)          | transmissivity of image dissector as a function of wave length                              |  |  |  |  |  |  |  |  |  |
| V             | velocity, km/sec  |  |  |  |  |  |  |  |  |  |
| M(y)          | Planck black-body function, watts/cm2 micron  |  |  |  |  |  |  |  |  |  |
| x             | coordinate along body axis, origin at wave apex, cm   |  |  |  |  |  |  |  |  |  |
| δ             | shock-wave standoff distance measured normal to surface, cm                                 |  |  |  |  |  |  |  |  |  |
| ψ             | angle between optical axis of image dissector and bore sight of the launching gun, deg      |  |  |  |  |  |  |  |  |  |
| θ             | angle from body stagnation point to local point on body surface, $180 \text{s}/\pi R$ , deg |  |  |  |  |  |  |  |  |  |
|               |   |  |  |  |  |  |  |  |  |  |





| φ | angle | between  | optical | axis | of | the | image | dissector | and | normal | to | body |
|---|-------|----------|---------|------|----|-----|-------|-----------|-----|--------|----|------|
|   | surf  | ace, deg | 5       |      |    |     |       |           |     |        |    |      |

- $\mu$  total absorption coefficient of hot air as defined in reference 1
- ρ density, gm/cm<sup>3</sup>

#### Subscripts

- e edge or shoulder of body
- s at the shock wave
- o standard atmospheric conditions
- stag stagnation point
- ∞ free-stream conditions

#### APPARATUS

#### Ballistic Range

High-speed conditions for the tests were obtained in a short ballistic range equipped with a deformable-piston light-gas gun (ref. 4). Standard range equipment included a number of shadowgraph stations and accompanying electronic counters for determining model attitude, position, and velocity at each shadowgraph station. Radiation data for the investigation were obtained with the image dissector described below.

#### Image Dissector

The image dissector, shown schematically in figure 1, was mounted downrange of a shadowgraph station. A mirror, located inside the test chamber, directed radiation from the hot gas in the shock layer through a lens, thus producing a near head-on image on an orifice plate. The motion of the model caused the image to move across the plate. The orifice plate contained an array of up to 20 holes arranged in 4 vertical columns as shown in the enlarged view in the figure. The holes were spaced in each column so that only one could receive radiation from the hot shock layer during any one test. Thus, model size and magnification of the optical system dictated hole spacing which varied from 3 to 10 millimeters. The vertical position of holes was staggered from column to column so that holes in various columns scanned lateral strips across the model face at different vertical heights. Behind each column was a lucite strip, 1.25 by 32 by 250





millimeters long, which carried the radiation to a photomultiplier tube. A time history of the radiation seen by each tube was recorded on an oscilloscope.

A lens, fl:2.5, with a 7-inch focal length was used to image the model and its associated luminous shock layer. The lens was mounted so that the model image was demagnified 2.9 times at the orifice plate. For a plate with 0.0127-cm diameter holes, the maximum ideal resolution was a spot 2.9x0.0127 = 0.0368 cm in diameter. Model diameters ranged from 1.525 to 0.762 cm. Therefore the spot size (i.e., resolving power) varied from about 2.5 to 5 percent of the model diameter. To minimize the loss of resolution for model positions away from the ideal object plane, the lens was stopped down to fl:16.

The dissector was alined after each test as described below. The mirror was adjusted so that the focused image of a small light source, placed on the gun bore sight, fell on the center hole in the second column of the orifice plate. Shadowgraphs of the light source recorded the height of the plane scanned by the hole. The relative position of the other holes in the orifice plate permitted calculation of the region scanned by each hole. Once the instrument was alined, the angle,  $\psi$ , between the optical axis and bore sight was computed. The angle varied between  $8^{\circ}$  and  $9^{\circ}$ .

To determine F, the fraction of radiation observed, the relative response of the system must be known. The transmissivities of the lens and plastic strips were measured separately. A relative response (fig. 2) of the entire system is determined from the combination of these transmissivities with the relative response of the photomultiplier tube. The mirror reflectance was considered to be constant over the range of wave lengths passed by other parts of the optical system. With the response,  $R(\lambda)$ , thus obtained, F can be computed from:

$$F = \frac{\Sigma R(\lambda) \mu_{T}(\lambda) W(\lambda)}{\Sigma \mu_{T}(\lambda) W(\lambda)}$$

The absorption coefficient  $(\mu_T)$ , taken from reference 5, is a function of temperature and density. Figure 3 shows F versus T for  $\rho_S/\rho_O$  of 0.1 and 1.0.

Since F is a function of the local temperature and density, it was necessary to determine whether it changed appreciably during a scan as a result of the variation of  $\rho$  and T with position across the model face. To this end, a sample calculation was made. For  $R/d=1.2,\,V_{\infty}=7.0$  km/sec, and at a density ratio  $\rho_{\infty}/\rho_{O}=0.013$  the equilibrium temperature and density and, consequently, the value of F were computed just behind the bow shock and along the streamline over the body surface from the stagnation point to the body edge. Figure 4 shows the results of this calculation. The fraction F is found to vary a maximum of about 15 percent at the shock wave and about 3 percent along the body. Therefore, in the analysis of the data, it was assumed to be constant.

The relative sensitivity of various holes in the image dissector together with their associated plastic strips and photomultiplier tubes was individually determined by means of a standard tungsten ribbon lamp. The central portion of





the ribbon was imaged on each hole and the ouput recorded. All values were normalized to the sensitivity of the middle hole in the second column.

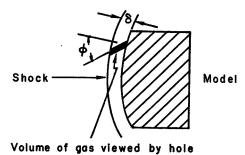
#### DATA REDUCTION PROCEDURE

The typical oscillograph recordings obtained during scans of model faces shown in figures 5(a), (b), and (c) illustrate changes in trace shape due to model nose shape and some consequences of signal pickup from the wake. The trace for a plastic sphere, figure 5(a), has a triangular shape while the trace for R/d = 1.2, figure 5(b), is more rounded. A major contribution to noise is from holes which do not scan the model face and therefore pick up signals from the wake during a scan. In figure 5(a), the signal-to-noise ratio is high because all holes but one in each column were covered for this test. Figure 5(b) shows a little lower signal-to-noise ratio with all holes open. In this latter case the noise level remained relatively low because the flight of a nonablating metal model with the resulting low intensity wake was observed. Figure 5(c) shows a high noise level trace. Here the model was an ablating plastic and all image dissector holes were open.

Two methods, depending on model nose shape, were used to relate sweep time on the oscilloscope trace to  $s/s_e$ . The horizontal plane scanned by each hole was determined from the alinement procedure described previously. Then the minimum value of  $s/s_e$  and chord length scanned by each hole was computed from shadowgraphs taken during the test. For the blunter shapes (flat faced and R/d=1.2), the radiation was fairly uniform across the entire face and dropped off rapidly at the edges. For these cases, the abrupt decrease in radiation was used to define the end points of the chord length scanned. Once the location of the edges was determined, the entire time scale on the trace was correlated to  $s/s_e$ . For the rounder models, the recorded intensity peaked sharply at the center of the scan. Therefore, correlation was based on the maximum reading corre-

was based on the maximum reading corresponding to the center of the chord scanned. Independent calculations of scan position along each strip, based on model velocity, trajectory, and viewing angle  $(\psi)$ , verified the selection of end points.

An intensity correction due to change in the volume seen during a scan was made for all except the flat-faced models. Radiation reaching a dissector hole at any time during a scan comes from a tube whose



length is approximated by  $\delta/\cos\phi$ , as shown in the sketch. Since the length  $\delta/\cos\phi$  changes significantly during a scan, the measured intensity is multiplied by  $\cos\phi$  at all points to correct for this effect. There is also a contribution of light scattered off the model face; this factor has little effect on the distribution of radiation intensity if the surface reflectivity is uniform as assumed.





The minimum value of  $s/s_e$  scanned (i.e., the closeness of scan line to the center of the model face) varied somewhat during the tests. For all tests except one (the sphere), the minimum value of  $s/s_e$  was such that the relative radiation distribution was within 3 percent of the maximum value at  $s/s_e = 0$ . In these cases, the data were plotted normalized to a value of 1 for  $s/s_e = 0$ . For R/d = 0.5, the data were normalized to the value of the relative distribution predicted by the theory (which will be discussed later) at the minimum value of  $s/s_e$  reached.

#### RESULTS AND DISCUSSION

The results of the present investigation in terms of the measured radiative intensity relative to the stagnation-point value are plotted in figures 6(a), (b), (c), and (d) as a function of  $s/s_e$ . Data presented are for bodies at  $0^O$  angle of attack. In all cases, the data are plotted so that reading from left to right on the figure corresponds to scanning the model face from the first edge which comes into view of the image dissector to the last edge. Notice that for R/d = 1.2, the results from both plastic and metal models show essentially the same intensity distribution. It is concluded, therefore, that radiation from ablation products (see, e.g., ref. 6) is not affecting the shape of the distributions.

Predicted radiation distributions are also indicated on these figures. Excluding the flat-faced body, these predictions are from reference 3 and represent the relative radiative flux falling on the body surface (i.e., the total radiation received by a point from all parts of the shock layer). This distinction between radiation falling on a surface element and that observed by the detector is important only when the gradient of intensity with distance along the scan changes rapidly. The surface flux is an average of radiation from a fairly large region of the shock layer while the present measurements yield more nearly local values in the gas. The presence of a sharp edge, which effects a rapid quenching, leads to a maximum discrepancy of about 30 percent. Therefore the difference between the measured and calculated distributions should be small, ranging from zero at the stagnation point to a maximum of 30 percent or less of the local flux at the edge.

The calculation of the distribution for the flat-faced model is described in detail in the appendix. It is based on numerical procedures similar to those used in reference 3.

The predictions shown on the figures indicate that the important variable influencing the nature of the radiation distribution is the nose shape, flight conditions being relatively unimportant. The calculations in reference 3 cover velocities from 8 to 16 kilometers per second and densities of approximately  $10^{-3}$  to  $10^{-4}$  standard atmosphere. The maximum variation of the distribution for a given body shape over this range of flight conditions is about 15 percent. Therefore the curves used in figures 6(a), (b), (c), and (d) are for average values of the distribution. Measurements also indicate nose shape to be the dominant variable over the range of flight conditions tested. In general, there





is good agreement between the calculations and experiment except for the R/d=0.65 shape. Since agreement exists for both more and less blunt shapes, and since poor correlation exists between the two tests in figure 6(c), the discrepancy is most probably due to model damage during launch although none was apparent from inspection of shadowgraph pictures. The apparent agreement for R/d=1.2 for large values of  $s/s_e$  is, in actuality, a modest disagreement, since the measured values should be somewhat higher than the predictions at the body edge.

To generalize the shape of the radiative distributions as a function of R/d, it is instructive to plot relative intensity versus  $\theta$  instead of s/s<sub>e</sub>. Figure 7 shows the calculated values from reference 3 replotted in this manner. It can be seen that the shape of the curve is essentially the same for all R/d as long as sonic flow is achieved on the body face. For cases where the sonic point is at the model edge (i.e., for bodies where the value of  $\theta$  at the corner is substantially less than about 38°), the curve will be similar at small values of  $\theta$  but will drop off faster as the effects of the edge become important. This is demonstrated for R/d = 1.2 for which  $\theta$  at the body corner is  $24^{\circ}$ .

#### CONCLUDING REMARKS

The distribution of the radiation relative to the stagnation-point flux has been measured across the faces of blunt axisymmetric bodies flying at hypersonic speeds and essentially 0° angle of attack. Over a range of bluntness from a hemisphere to a flat face, the measured distributions are in fair agreement with calculated distributions. It has been demonstrated that the important parameter is the nose shape; changes in model material tested and modest changes in flight conditions produced variations in the distribution smaller than the experimental scatter. The results of this work and the comparisons given herein offer convincing evidence that our present understanding of the distribution of thermal radiation from blunt-body bow shock regions in thermodynamic and chemical equilibrium is well founded.

Ames Research Center
National Aeronautics and Space Administration
Moffett Field, Calif., July 10, 1963





#### CALCULATION OF THE DISTRIBUTION OF RADIATION

#### FOR A FLAT-FACED BODY

The standoff distance at the stagnation point was determined from reference 7

$$\delta = 0.416 \, d/\sqrt{\rho_s/\rho_{\infty}}$$

and the shock shape from reference 8

$$r_s/d = 1.22 (x_s/d)^{0.303}$$

The oblique shock relations and the real gas charts of reference 9 were used to determine the temperature and density distributions just behind the shock wave. The temperature and density distributions along the body surface were approximated by assuming isentropic expansion from the stagnation point and by using an unpublished pressure distribution obtained from wind-tunnel data by Seiff and Stalder at Ames. This distribution is reproduced in figure 8. The temperature and density were assumed to vary linearly from shock to wall and average values computed as a function of s/se. In the temperature and density range for this test, reference 10 indicates that radiant flux varies approximately as the 1.3 power of the density and the 11 power of the temperature. Therefore, the relative intensity can be computed from

$$\frac{\text{I}(\text{s/s}_{\text{e}})}{\text{I}_{\text{stag}}} = \left[\frac{\overline{\text{T}}(\text{s/s}_{\text{e}})}{\text{T}_{\text{stag}}}\right]^{11} \left[\frac{\overline{\rho}(\text{s/s}_{\text{e}})}{\rho_{\text{stag}}}\right]^{1.3} \left[\frac{\delta(\text{s/s}_{\text{e}})}{\delta_{\text{stag}}}\right]$$

The results are given in figure 6(a). Because the variation of temperature and density from shock to wall is small, the error incurred in using average values of these variables is about 1 percent.





#### REFERENCES

- 1. Canning, Thomas N., and Page, William A.: Measurements of Radiation From the Flow Fields of Bodies Flying at Speeds Up to 13.4 Kilometers per Second. Presented to the Fluid Mechanics Panel of Advisory Group for Aeronautical Research and Development, Brussels, Belgium, April 3-6, 1962.
- 2. Page, William A.: Shock-Layer Radiation of Blunt Bodies Traveling at Lunar Return Entry Velocities. IAS Paper 63-41.
- 3. Wick, Bradford H.: Radiative Heating of Vehicles Entering the Earth's Atmosphere. Presented to the Fluid Mechanics Panel of Advisory Group for Aeronautical Research and Development, Brussels, Belgium, April 3-6, 1962.
- 4. Curtis, John S.: An Accelerated Reservoir Light-Gas Gun. NASA TN D-1144, 1962.
- 5. Meyerott, R. E., Sokoloff, J., and Nicholls, R. W.: Absorption Coefficients of Air. Lockheed Aircraft Corporation, Missiles and Space Division, IMSD-288052, Sept. 1959.
- 6. Craig, Roger A., and Davy, William C.: Thermal Radiation From Ablation Products Injected Into a Hypersonic Shock Layer. NASA TN D-1978, 1963.
- 7. Probstein, Ronald F.: Inviscid Flow in the Stagnation Point Region of Very Blunt-Nosed Bodies at Hypersonic Flight Speeds. Brown University, WADC TN-56-395, Sept. 1956.
- 8. Seiff, Alvin, and Whiting, Ellis E.: A Correlation Study of the Bow-Wave Profiles of Blunt Bodies. NASA TN D-1148, 1962.
- 9. Feldman, Saul: Hypersonic Gas Dynamics Charts for Equilibrium Air. AVCO-Everett Research Laboratory, Res. Rep. 40, Jan. 1957.
- 10. Kivel, Bennett: Radiation from Hot Air and Stagnation Heating. AVCO-Everett Research Laboratory, Res. Rep. 79, Oct. 1959.





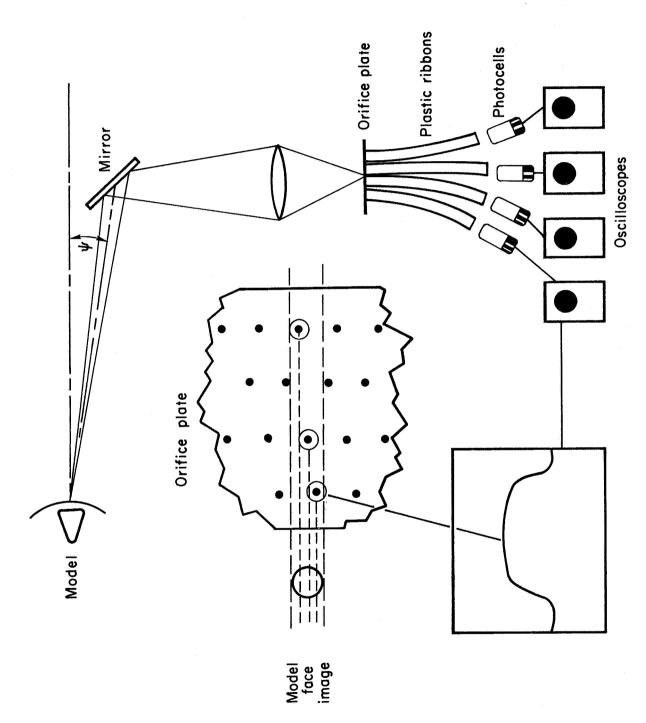


Figure 1.- Schematic drawing of image dissector.

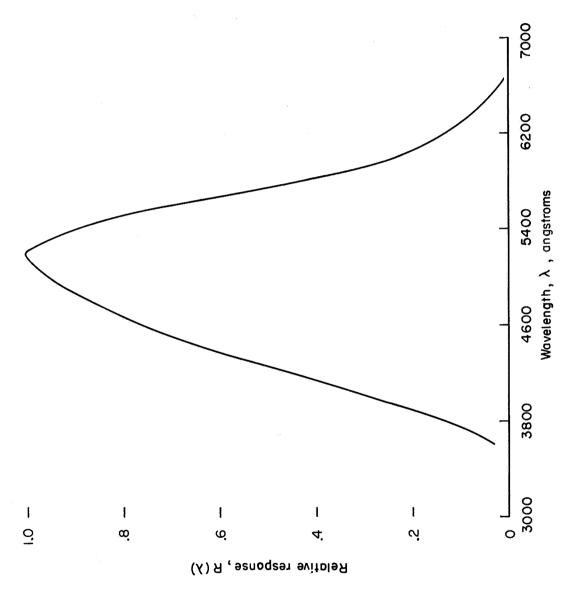
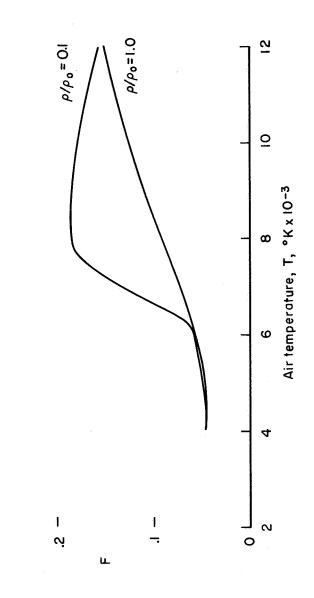


Figure 2.- Typical relative spectral response of dissector

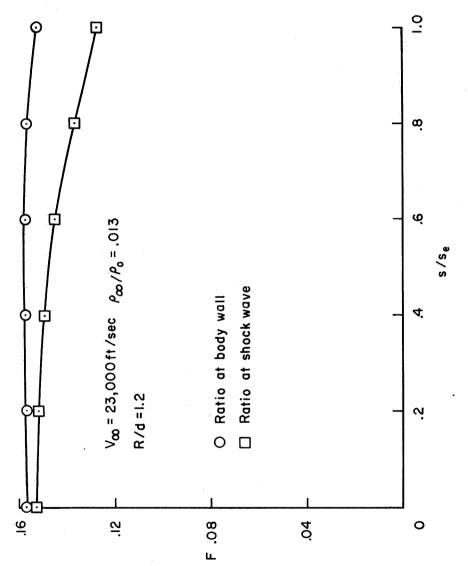




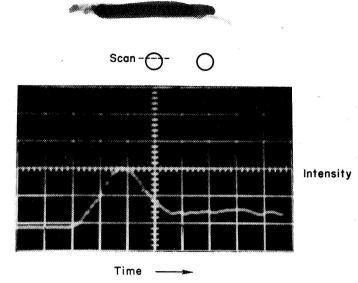
نن ا

Figure 3.- Portion of total radiation to which image dissector is sensitive.

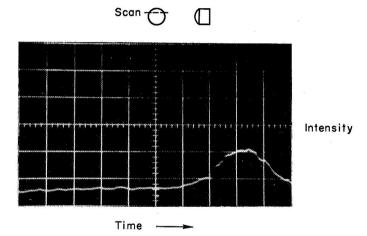




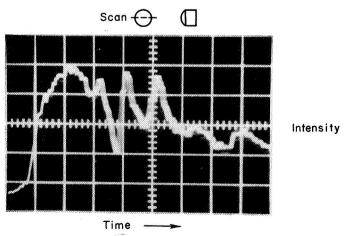
F within the gas cap of a typical model. Figure 4.- Variation of



(a) Plastic sphere; R/d = 0.5; one hole open.



(b) Metal model; R/d = 1.2; all holes open.



(c) Plastic model; R/d = 1.2; all holes open.

Figure 5.- Image dissector oscilloscope trace.



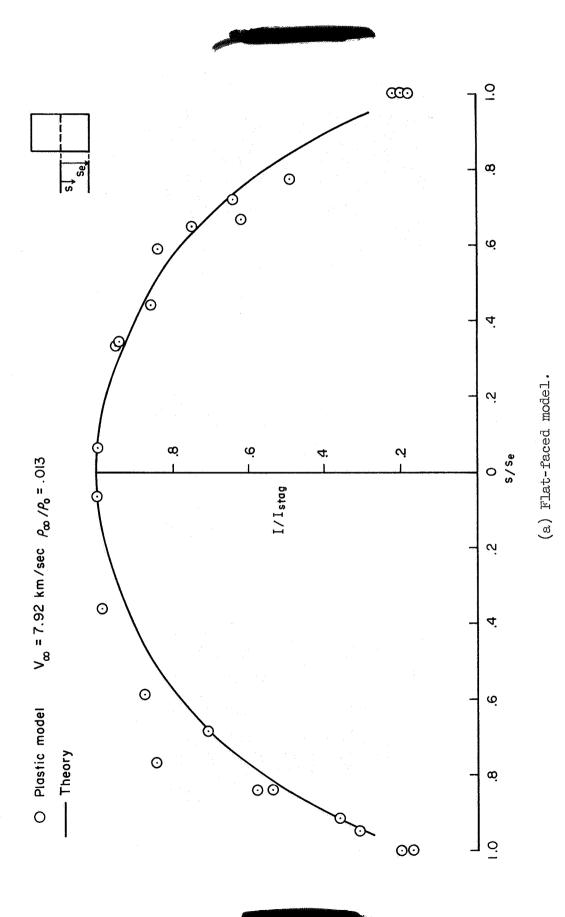
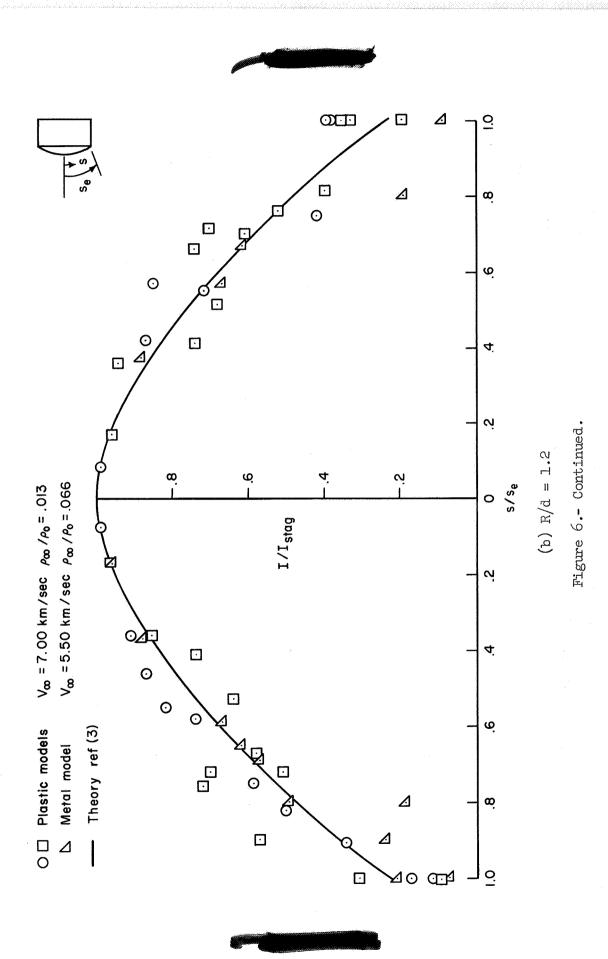
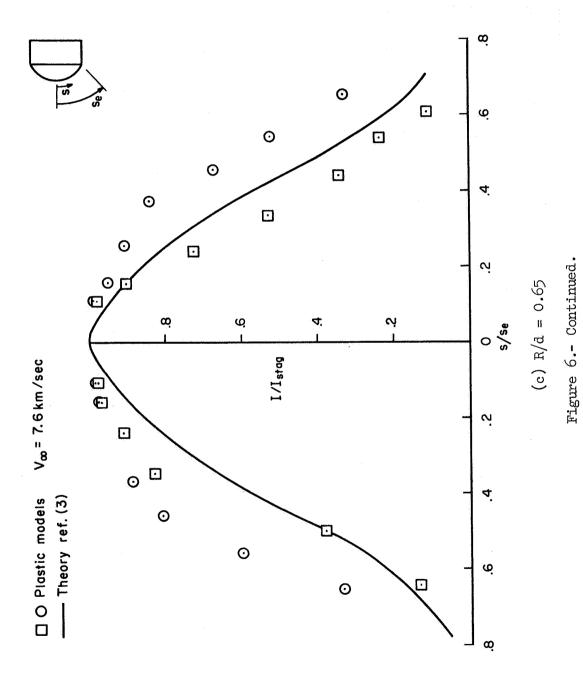
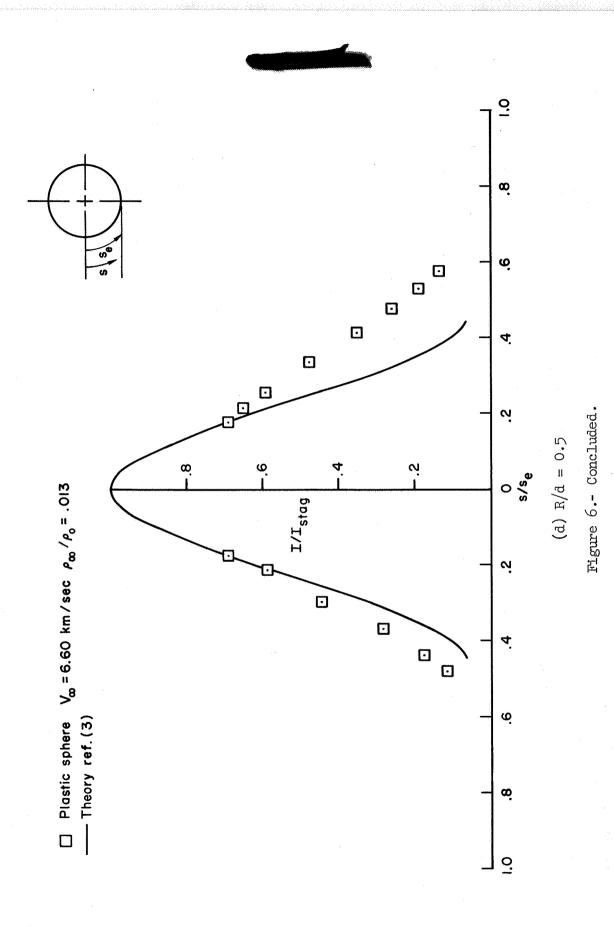


Figure 6.- Measured distributions of radiation intensity.









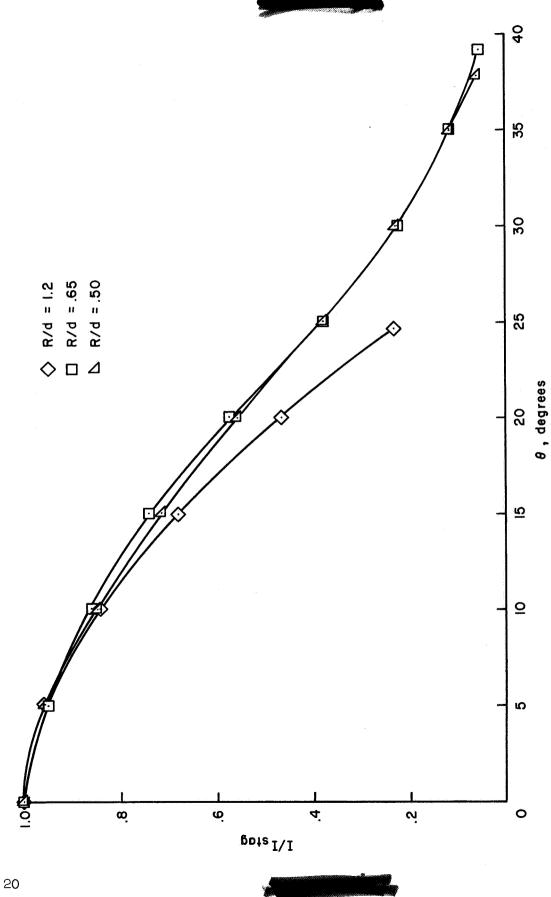


Figure 7.- Theoretical radiation distribution as a function of  $\ensuremath{\mathrm{R}}/\ensuremath{\mathrm{d}}\xspace.$ 

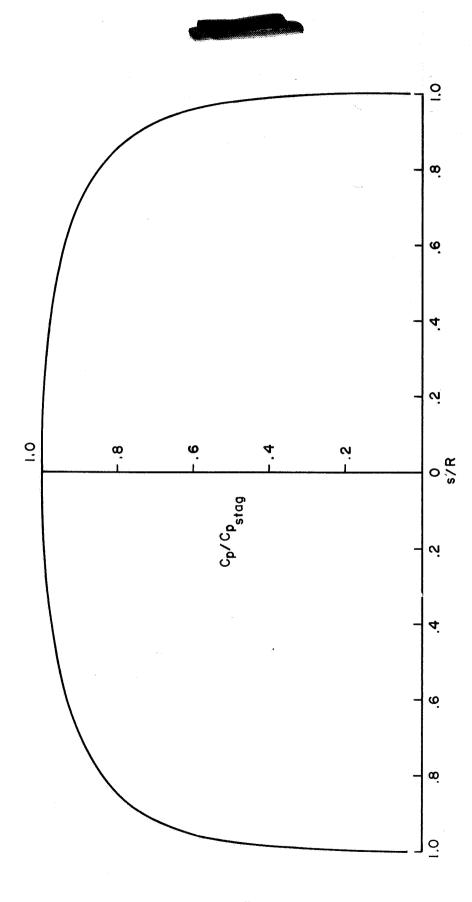


Figure 8.- Relative pressure distribution on flat face of circular-cylinder; M=2.4.

NASA-Langley, 1963 A-825

21